HD 265435: a new super-Chandrasekhar candidate supernova progenitor

Ingrid Pelisoli[1*], **S. Geier**[1], **P. Neunteufel**[2], **T. Kupfer**[3,4], **U. Heber**[5], **A. Irrgang**[5], **D. Schneider**[5], **A. Bastian**[1], **J. van Roestel**[6], **V. Schaffenroth**[1], **and B. N. Barlow**[7]

[1]Institut für Physik und Astronomie, Universität Potsdam, Haus 28, Karl-Liebknecht-Str. 24/25, D-14476 Potsdam-Golm, Germany
[2]Max Planck Institut für Astrophysik, Karl-Schwarzschild-Straße 1, 85748 Garching bei München
[3]Kavli Institute for Theoretical Physics, University of California, Santa Barbara, CA 93106, USA
[4]Texas Tech University, Department of Physics & Astronomy, Box 41051, 79409, Lubbock, TX, USA
[5]Dr. Karl Remeis-Observatory & ECAP, Astronomical Institute, Friedrich-Alexander University Erlangen-Nuremberg (FAU), Sternwartstr. 7, 96049 Bamberg, Germany
[6]Division of Physics, Mathematics and Astronomy, California Institute of Technology, Pasadena, CA 91125, USA
[7]Department of Physics and Astronomy, High Point University, High Point, NC 27268, USA
[*]pelisoli@astro.physik.uni-potsdam.de

ABSTRACT

Supernova Ia are bright explosive events that can be used to estimate cosmological distances, allowing us to study the expansion of the Universe. They are understood to result from a thermonuclear detonation in a white dwarf, the exhausted core of a Sun-like star. However, the possible progenitor channels leading to an explosion are a long-standing debate, limiting the precision and accuracy of supernova Ia as distance indicators. Here we present HD 265435, a binary system with an orbital period of less than a hundred minutes, consisting of a white dwarf and a hot subdwarf — a stripped core-helium burning star. The total mass of the system is 1.6 solar-masses, exceeding the Chandrasekhar limit (the maximum mass of a stable white dwarf). The system will merge due to gravitational wave emission in 79 million years, triggering a supernova Ia event. We use this detection to place constraints on the contribution of hot subdwarf-white dwarf binaries to supernova Ia progenitors.

Type Ia supernovae (SN Ia) represent one of the crucial rungs on the cosmic distance ladder. As bright standard candles, they are essential tools in obtaining measurements of the Hubble constant H_0, which describes how fast the Universe is expanding at different distances, allowing us to model and comprehend the structure and evolution of the Universe[1–3]. An accurate determination of the systematic uncertainties involved in these cosmological measurements requires a reliable identification of the progenitor channels contributing to the observed SN Ia population. Current measurements of H_0 in the local Universe relying on SN Ia[4] are inconsistent with estimates using the cosmic microwave background radiation observed by the Planck experiment[5]. In order to establish whether this H_0 tension[6] is evidence for new Physics, or rather a consequence of poor determination of systematic uncertainties, it is imperative to understand possible SN Ia channels and their relative contributions

Although the origin of SN Ia has for long been understood as a thermonuclear detonation in a white dwarf[7], triggered when a critical mass near the Chandrasekhar limit of 1.4 $M_\odot$[8] is reached, the mechanism for the explosion itself remains under debate[9]. Possible channels for achieving critical mass can be generally grouped in two: double degenerate, or single degenerate. In the double degenerate channel, the white dwarf has another compact star as a companion, and the detonation is triggered by the merger of the two objects[10–12]. In the single degenerate channel, the white dwarf accretes mass from a companion up to a point in which thermonuclear explosion is triggered[10,13]. Confirmed progenitors are extremely scarce for both channels[14], making it challenging to explain observed rates[15]. The once promising Henize 2-428 system[16] has recently been shown to have a total mass significantly lower than previously derived, and can no longer be considered as a SN Ia progenitor[17]. Even in the dedicated ESO supernovae type Ia progenitor survey (SPY), only two systems (WD2020-425 and HE2209-1444) have been identified as possible progenitors, both with sub-Chandrasekhar total masses[18]. The only known super-Chandrasekhar candidate progenitor is KPD 1930+2752[19,20], a hot subdwarf with a close white dwarf companion. Another similar albeit less massive binary, CD-30°11223[21,22], also qualifies as SN Ia progenitor. These merging massive systems can also be of interest as gravitational wave sources, in particular as verification sources for the upcoming Laser Interferometer Space Antenna (*LISA*)[23].

Here we report the discovery that HD 265435 is a candidate supernova progenitor and *LISA* verification binary composed by a hot subdwarf with a massive white dwarf companion. This $V = 11.78$ binary system is at a distance of less than 500 pc from the Sun, making it the closest super-Chandrasekhar candidate supernova progenitor. We analysed the light curve obtained by the Transiting Exoplanet Survey Satellite (TESS)[24] together with time-series spectroscopy to characterise the system and determine the component masses. The properties of this binary make it a candidate for both the single degenerate and double degenerate SN Ia channels.

Results

HD 265435 (TIC 68495594) was observed by TESS in Sector 20. The data revealed ellipsoidal variation with a period of 100 minutes, suggesting that the visible component of the system is tidally deformed by a compact object. Following this discovery, we obtained time-series spectroscopy at the Palomar 200-inch telescope with the Double-Beam Spectrograph (DBSP)[25] covering one orbital cycle, with the aim of obtaining the radial velocity curve of the visible star. We also obtained a high-resolution spectrum with the Echellette Spectrograph and Imager (ESI) at the Keck II telescope to determine the line-of-sight rotational velocity, $v \sin i$. Combining the spectra with the radius estimate from fitting the spectral energy distribution (SED) using the *Gaia* data release 2 (DR2)[26] parallax, we completely characterised the visible component, a hot subdwarf of spectral type B (sdB). The analysis of the TESS light curve, together with the radial velocity curve of the sdB, allowed us to infer the mass of the unseen companion, which is likely a white dwarf with a carbon-oxygen core. The obtained stellar and binary parameters for HD 265435 are provided in Table 1.

Table 1. Stellar and binary parameters for HD 265435. The sdB radius was determined via SED fit. The effective temperature ($T_{\rm eff}$), logarithm of surface gravity ($\log\ g$), and logarithm of helium over hydrogen abundance ($\log\ y$) were determined by spectroscopic fit. The sdB mass was obtained from the $\log\ g$ and radius. The companion mass combines constraints from the light curve and radial velocity fits. Ephemeris, the mass ratio $q = M_{\rm comp}/M_{\rm sdB}$, and the inclination i resulted from the light curve fit. The orbital separation a was calculated from the light curve fit and sdB radius. The merging time τ and gravitational wave amplitude $\mathscr{A}$ were calculated using the derived masses and orbital period. Quoted values are the median and uncertainties give the 68% confidence interval.

Parameter	Hot subdwarf	Compact companion
RA (J2000)	06:53:24.30	
DEC (J2000)	+33:03:34.2	
V	11.78 ± 0.18[27]	
G	12.1069 ± 0.0022[26]	
ϖ (mas)	2.20 ± 0.06[26]	
μ_α (mas/yr)	-4.60 ± 0.10[26]	
μ_δ (mas/yr)	-4.52 ± 0.09[26]	
Mass ($M_\odot$)	$0.52^{+0.09}_{-0.08}$	1.02 ± 0.09
Radius ($R_\odot$)	0.204 ± 0.007	-
$T_{\rm eff}$ (K)	33640 ± 640	-
$\log\ g$ [cgs]	5.54 ± 0.06	-
$\log\ y$	-1.57 ± 0.14	-
T_0 (BJD)	24571909.6899552(26)	
P (days)	0.0688184888(32)	
K (km/s)	342 ± 7	-
V_0 (km/s)	8 ± 5	
q	$1.65^{+0.11}_{-0.09}$	
i (degrees)	$59.9^{+2.4}_{-2.1}$	
a ($R_\odot$)	$0.701^{+0.035}_{-0.032}$	
τ (Myr)	79^{+14}_{-11}	
$\mathscr{A}$	$2.98^{+0.51}_{-0.44} \times 10^{-22}$	

Period determination

A Lomb-Scargle periodogram[28,29] of the TESS light curve showed a dominant peak at 49.54959(15) min (Fig. 1). Phase-folding the light curve to twice this dominant peak revealed the occurrence of Doppler boosting[30], causing a height difference of $\approx 0.3\%$ between consecutive maxima, indicating that the real orbital period is $P = 99.09918(29)$ minutes. A smaller amplitude peak can be seen at this period, as well as harmonics at P/3 and P/4. The periodogram also shows a wealth of short-period peaks, consistent with p-mode pulsations of the hot subdwarf[31,32]. We identified a total of 33 frequencies above a detection level of five times the average amplitude of the Fourier transform (see Supplementary Table 2). Many of these frequencies are part of rotational multiplets, which are separated by the orbital period (see Supplementary Figure 6), suggesting that the rotation period of the subdwarf is equal to the orbital period, i.e. the system is synchronised, as is often is observationally inferred for sdB binaries with orbital periods of less than half a day[33].

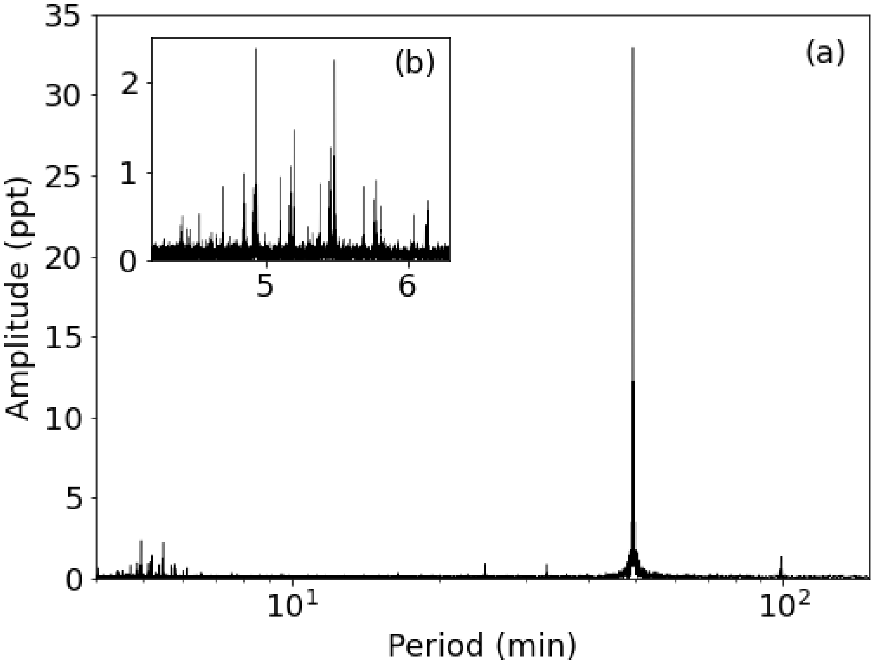

Figure 1. Periodogram of the TESS light curve. Panel (a) shows the full periodogram, in which a dominant peak can be seen at 49.54959(15) min, corresponding to half the orbital period. Multiple low-period peaks can also be identified in the range of 4–6 minutes, as detailed in the inset panel (b).

The TESS 2-minute cadence is not adequate for correctly sampling p-mode pulsations, therefore we attempt no asteroseismologial analysis. The pulsation frequencies were identified so that the effect of the pulsations could be subtracted from the light curve prior to modelling the effect of the binary companion, otherwise they would have lead to systematic errors on the final fit parameters. This was done recursively: we first calculated a preliminary model for the variability due to binarity (see Methods for details), which we then subtracted from the original light curve in order to determine the pulsation frequencies. Next we performed a global fit using all 33 identified frequencies, and subtracted the obtained model from the original light curve. The preliminary model was also used to fit the full light curve in order to refine the period and determine the zero point of the ephemeris (adopted here as the superior conjunction of the unseen companion). We obtained a period of $P = 0.0688184888(32)$ days, and $BJD_0 = 24571909.6899552(26)$ days. The light curve and radial velocity data folded using this ephemeris is shown in Fig. 2.

The radial-velocity curve of the hot subdwarf

We determine the radial velocities by cross-correlating each spectrum obtained with DBSP with a best-fit spectral template (see the Methods for a full description of the procedure). We analysed spectra from the blue and red arms separately, as they are not obtained simultaneously, and obtained consistent radial velocities. We fitted the radial velocities assuming a circular orbit, with the period fixed to the photometric period, as the time span of our radial velocity curve would not allow a precise independent determination of the period. We allowed the zero point of the ephemeris to vary by P/2 in order to account for possible phase shifts between the photometric and spectroscopic data, obtaining a value consistent with the photometry within three decimal cases. The best-fit model is shown in the bottom panel of Fig. 2. The obtained radial velocities revealed a large radial semi-amplitude of $K_{\rm sdB} = 342 \pm 7$ km s^{-1}, implying in a mass function for the unseen companion of

$$f_{\rm comp} = \frac{P K_{\rm sdB}^3}{2\pi G} = 0.288^{+0.020}_{-0.019}\, M_\odot. \quad (1)$$

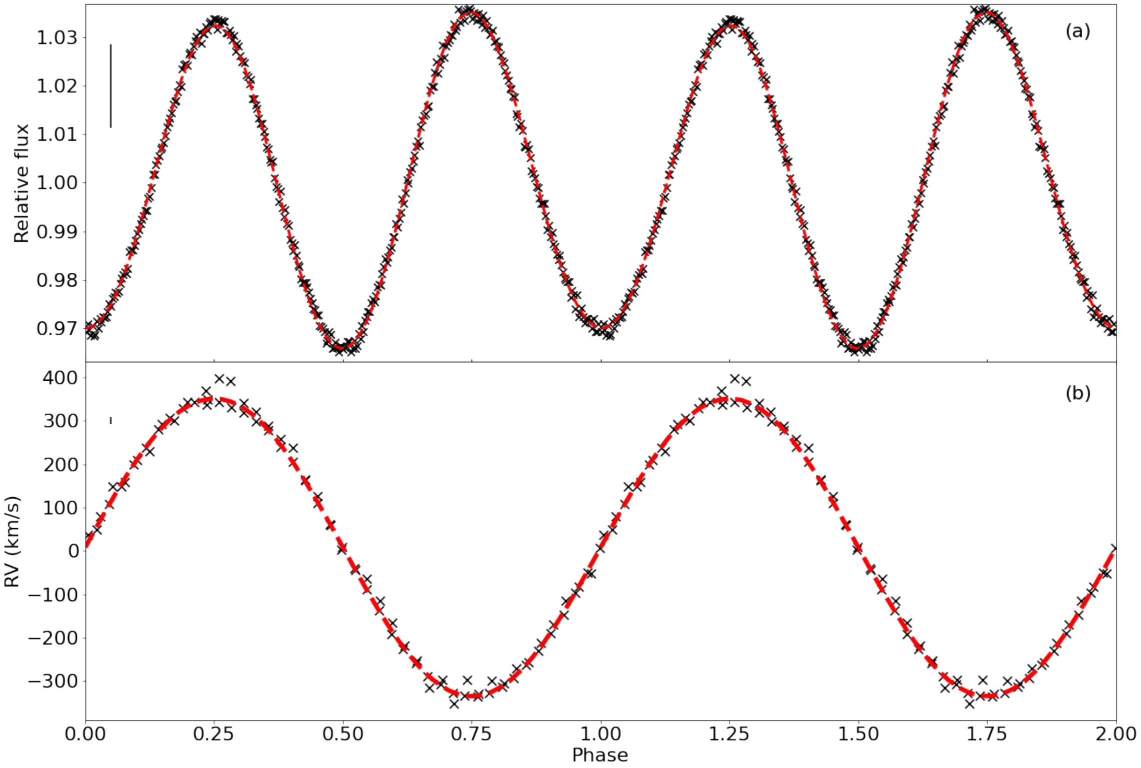

Figure 2. Phased data for HD 265435. Panel (a) shows the light curve, and panel (b) the radial velocity data, both phase-folded to the obtained ephemeris. The data is shown as crosses, and our best-fit models are shown as red dashed lines. Bars to the top left show the median measurement uncertainties in each case. The dominant effect in the light curve is an ellipsoidal variation caused by the tidal deformation of the visible component. The tidal deformation also leads to gravity darkening, causing the two minima to show different depths. The less prominent effect of Doppler boosting, which causes maxima to show different heights, is in turn caused by the orbital motion of the visible companion.

Combining the obtained systemic velocity with the *Gaia* DR2 astrometric information, we find the system to show dynamics consistent with the thin disk of the Galaxy (see Methods for details).

Hot subdwarf stellar parameters

The obtained spectra revealed the visible component to be a sdB, as already suggested based on its *Gaia* DR2 parameters[34]. We performed a spectral fit of the Doppler corrected and co-added DBSP spectrum (as detailed in the Methods section), obtaining an effective temperature of $T_{\rm eff} = 33640 \pm 640$ K and surface gravity with $\log\ g = 5.54 \pm 0.06$. These values were fixed when fitting the high-resolution ESI spectrum, allowing us to determine $v \sin i = 152 \pm 7$ km s^{-1} and helium-to-hydrogen ratio (by number) $\log y = -1.57 \pm 0.14$.

Performing a fit to the SED (see Methods for further details), we find the photometry to be consistent with a single hot subdwarf, finding no contribution from the unseen companion. Using the *Gaia* DR2 parallax, our SED fit provided a radius estimate of $R_{\rm sdB} = 0.204 \pm 0.007\ R_\odot$, implying a hot subdwarf mass of $0.52^{+0.09}_{-0.08}\ M_\odot$ given the obtained $\log\ g$. With the mass function calculated above, this implies a minimal mass for the companion of $M_{\rm comp} > 0.80\ M_\odot$, corroborating its nature as a compact object, as no contribution from an early-type companion is observed.

The mass of the unseen component

The compact object is not eclipsing, nor contributing significantly to the detected light, therefore its temperature and radius cannot be determined. Its mass, on the other hand, can be constrained given the observable effects of a companion on the hot subdwarf, namely the tidal deformation and radial velocity variability.

We fit the light curve using LCURVE[35], a code that uses a grid of points to model the brightness of two orbiting stars with shapes set by a Roche potential. We left as free parameters the mass ratio q, the inclination angle i, the scaled radius of the hot subdwarf $r_{\rm sdB} = R_{\rm sdB}/a$, where a is the orbital distance, and the velocity scale, $V_{\rm scale} = (K_{\rm sdB} + K_{\rm comp})/\sin\, i$ (see Methods for details on the procedure). The log g of the hot subdwarf was required to be consistent with the spectroscopic value, the inclination was required to be consistent with the measured $v \sin i$, since the hot subdwarf is tidally-locked, and the value of $K_{\rm sdB}$ was required to be consisted with the determination from the radial velocity observations. Combining the fitted mass ratio with the derived hot subdwarf mass, the mass of the unseen companion can be determined from the tidal deformation. The radial velocity variability of the hot subdwarf gives a second constraint through the binary mass function,

$$f_{\rm comp} = \frac{q^2 M_{\rm comp} \sin^3(i)}{(1+q)^2}. \tag{2}$$

Combining both constraints by multiplying the probability density functions resulting from each case (see Fig. 3), we obtain the mass of the companion to be $M_{\rm comp} = 1.02 \pm 0.09\, M_\odot$. This implies that the companion is likely a white dwarf with a C/O core, although an O/Ne(/Mg) composition is possible if the mass is above 1.088 $M_\odot$[36]. The total mass of the system is found to be $1.57^{+0.13}_{-0.12}\, M_\odot$.

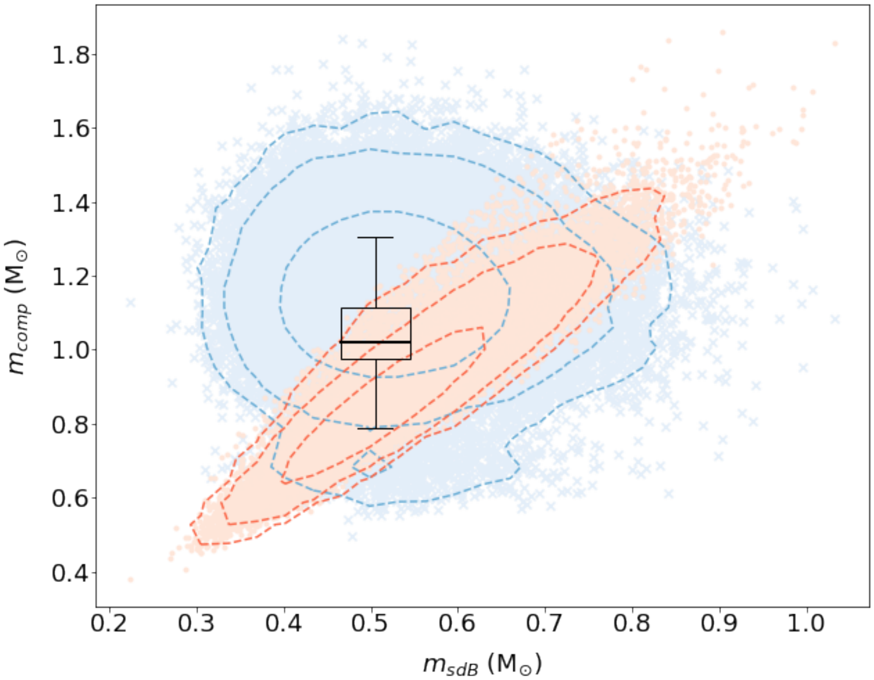

Figure 3. Mass estimate for the unseen companion. Blue crosses indicate the mass calculated using the binary mass function, whereas q and the sdB mass alone were used for the red dots. Dashed lines indicate confidence levels of 68, 95, and 99%. The boxplot indicates the adopted mass combining both constraints – the box represents the 68% confidence interval, with the median marked as a line, and the bars span the 95% confidence interval.

Future evolution of HD 265435

The evolution of the binary is primarily determined by the total mass of the system, initial orbital separation and the evolutionary status of the hot subdwarf at the time of Roche-lobe overflow (RLOF). The obtained radius of the hot subdwarf is larger than that of a typical pure helium sdB of the same mass[37], which hints at the presence of a thin remnant hydrogen-rich envelope[38]. A less likely alternative, considering the timescales, is that the hot subdwarf is still contracting following a common-envelope (CE) phase. In this case, the remnant hydrogen envelope would likely be less massive to nonexistent.

We carried out a numerical simulation of the evolution of the system in order to determine its possible outcomes. The hot subdwarf was modelled by an evolved helium star with solar metallicity, giving physical parameters consistent with the observed values (see top panel of Fig. 4). The model was placed in a binary with a carbon-oxygen core white dwarf approximated by a point mass. We include the effects of rotation, assuming tidal locking, angular momentum loss through gravitational radiation and wind. RLOF-driven mass transfer is assumed to be conservative. Further details of the simulation are given in the Methods section.

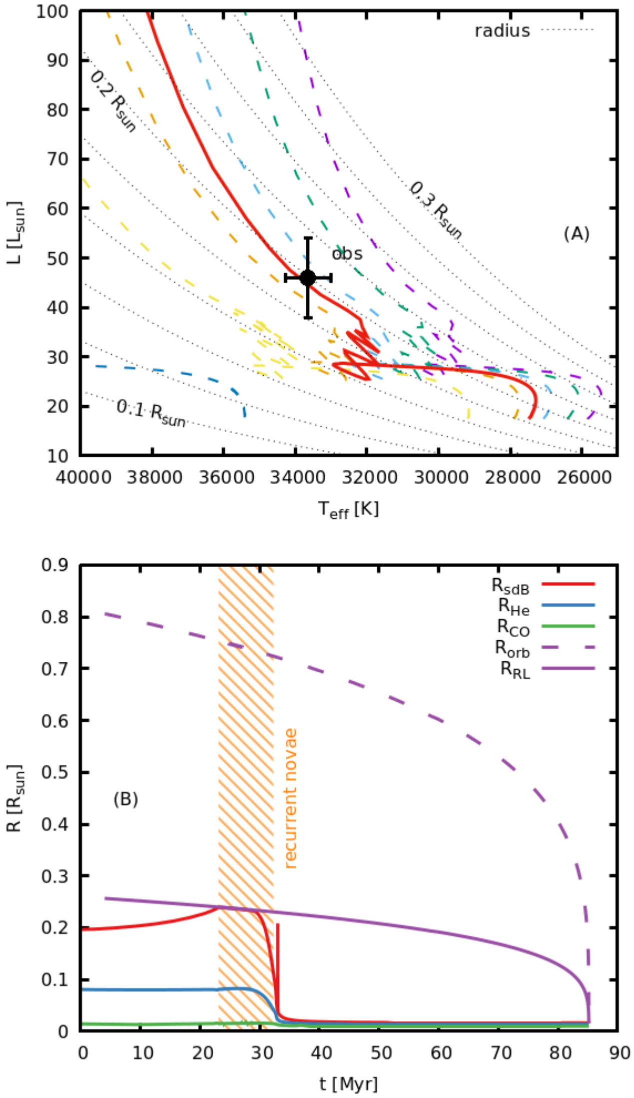

Figure 4. Model and prediction of the future evolution of HD265435. Panel (A) shows predicted evolutionary tracks for sdBs of a mass of $0.50\,M_\odot$ and H-envelopes between $0.0005\,M_\odot$ and $0.0015\,M_\odot$ with the solid line representing the favoured model with $0.001\,M_\odot$. The sdBs observed position in the diagram, including error bars, is as indicated. Lines of constant radius are given for orientation. Panel (B) shows the orbital evolution of the system. Here, R_{sdB} is the total radius of the sdB, including hydrogen envelope. R_{He} is the radius of the He-rich shell and R_{CO} the radius of the inert CO core. R_{RL} is the radius of the Roche lobe of the sdB. The hatched area indicates the expected phase of recurrent nova outbursts.

Our model indicates that the loss of angular momentum through the emission of gravitational radiation will lead to RLOF after ~ 20 million years. In the preferred scenario, the transferred material will be hydrogen enriched, and the mass transfer rates may be sufficient to lead to a series of classical nova outbursts by the accreting white dwarf[39,40] (see bottom panel of Fig. 4).

Considering the alternative scenario, in which the large radius of the hot subdwarf results from a recent common-envelope phase, there would be a phase of helium-rich mass transfer onto the white dwarf. We find the rates to be initially low enough to allow for quiescent accumulation of the helium enriched material. This helium layer can act as a detonator, triggering a single-degenerate SN Ia or SN Iax, through what is known as a double detonation scenario[41–43]. However, we find that the mass transfer raters increase above the estimated limit for quiescent accumulation[44,45] before sufficient helium has been accumulated, which would lead to a massive helium nova leaving the white dwarf carbon-oxygen core largely intact. Therefore, a single degenerate supernova is only a marginal possibility.

The derived masses allow us to constrain the merger time due to gravitational wave emission[46], which is found to be 79^{+14}_{-11} Myr, consistent with our numerical simulation. The characteristic strain[47,48] of the system places it above the detection limit of *LISA*, as illustrated in Fig. 5. The merger of the two stars will result in a double-degenerate thermonuclear supernova.

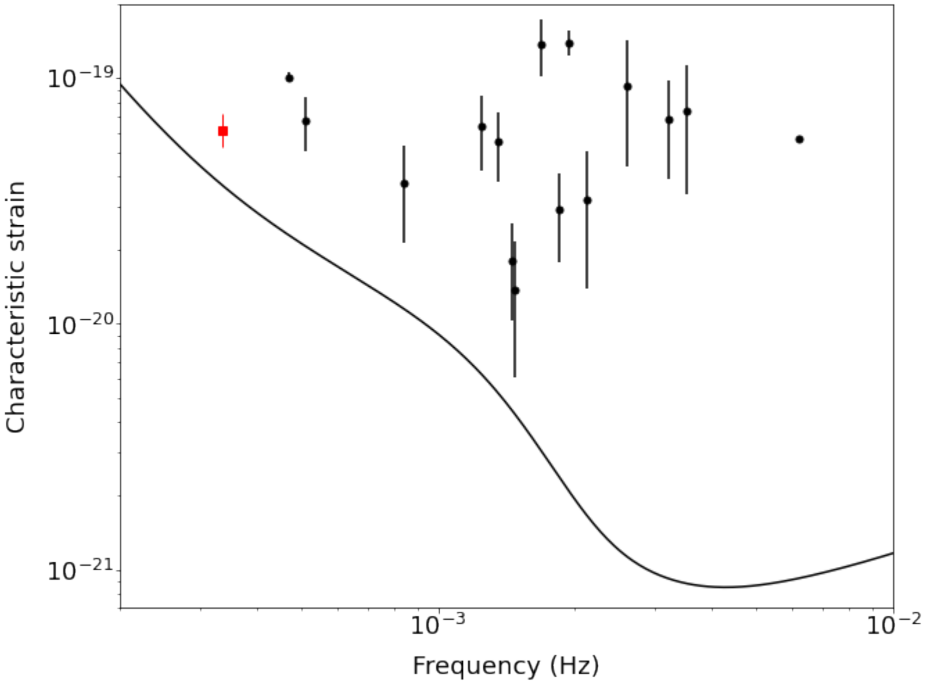

Figure 5. Gravitational wave frequency and strain of HD 265435. The black line shows the *LISA* sensitivity curve for a four-year mission[49]. The red square shows the strain and frequency of HD 265435. Black data points are previously known verification binaries[50].

Discussion

The newly discovered system HD 265435 brings the number of hot subdwarf with white dwarf companions that qualify as SN Ia progenitors to three, making this the class of binaries with the most observed progenitor candidates. HD 265435 has very similar properties to KPD 1930+2752: both harbour a relatively hot sdB star ($T_{\rm eff} > 30\,000$ K) and a massive white dwarf with a CO core as companion, bringing the total mass of the system above the Chandrasekhar limit. Additionally, both sdBs in HD 265435 and in KPD 1930+2752 have been observed to show *p*-mode pulsations. CD-30° 11223, on the other hand, has lower mass components and total mass slightly below the Chandrasekhar limit. However, KPD 1930+2752 will likely evolve through the core-He burning phase without filling its Roche lobe and transferring mass to the companion[51], whereas mass transfer is predicted to happen to both HD 265435 and CD-30° 11223. Therefore, in terms of its evolutionary fate, HD 265435 is more similar to CD-30° 11223. A class of Roche lobe-filling hot subdwarf binaries has recently been discovered[52,53], providing observational evidence for the existence of systems undergoing mass transfer before the hot subdwarf evolves into a white dwarf.

Perhaps the most remarkable common property of these candidate supernova progenitors is the fact that they are all found within 1 kpc of the Sun and seem to be members of the thin disk. Given their *Gaia* DR2 parallaxes, CD-30°11223 is at 337 ± 9 kpc, HD 265435 at 455 ± 13 pc, and KPD 1930+2752 at 876^{+39}_{-36} pc. Making the assumption that these three objects consist of the entire sample of hot subdwarf-white dwarf binaries that qualify as supernova progenitors within 1 kpc, that would imply a space density of 0.22 kpc^{-3} for this type of system, considering the effective volume given by the thin disk density[54]. We can also roughly estimate the rate of SN Ia that can be attributed to such systems. There are ~ 3000 hot subdwarf candidates within 1 kpc[34]. Accounting for an estimated contamination level of 10%[34], this would suggest that 3 out of the 2700 hot subdwarfs within 1 kpc are possible SN Ia progenitors. Given the birthrate of such stars of $\sim 5 \times 10^{-2}$ yr^{-1}[55], this implies that the SN Ia rate that can be attributed to hot subdwarf-white dwarf binaries is 5×10^{-5} yr^{-1}. Population synthesis simulations suggest a larger value of 3×10^{-4} yr^{-1} for the contribution of helium star-white dwarf binaries to the SN Ia rate[56], but this estimate includes also helium stars more massive than hot subdwarfs. The Galactic SN Ia rate is in turn estimated to be $7.2 \pm 2.3 \times 10^{-3}$ yr^{-1}[57,58]. Therefore, our estimate suggests that hot subdwarf-white dwarf binaries do not contribute significantly to the Galactic SN Ia rate, despite being the most numerous observed class of progenitors. Our estimate should be, however, regarded as a lower limit, since we have assumed that there are no other SN Ia progenitors consisting of hot subdwarf-white dwarf binaries within 1 kpc. The TESS extended mission, as well as future missions such as the Legacy Survey of Space and Time (LSST), will put this assumption to test.

Methods

Observations and data reduction

HD 265435 (TIC 68495594) was observed by TESS in Sector 20, yielding two-minute cadence data over a baseline of 26.3 days, with a three day gap after 12.3 days during which the data were being downloaded to Earth. We retrieved the light curve derived by the TESS Science Processing Operations Center (SPOC), and used the PDCSAP flux, which corrects the simple aperture photometry (SAP) to remove instrumental trends and contributions to the aperture expected to come from neighbouring stars identified in a pre-search data conditioning (PDC). The pipeline also provides an estimate of the contribution of the target to the flux in the aperture, taking into account possible contamination by neighbouring targets. The value for HD 265435 is 0.65. The contamination is likely due to a $G = 12.3$ star 28" away[1]. This much redder star ($G_{BP} - G_{RP} = 0.786$, compared to $G_{BP} - G_{RP} = -0.469$ for HD 265435) is likely a main sequence F star given the stellar parameters in the *Gaia* DR2 ($T_{\mathrm{eff}} = 5860$ K and $R = 1.50\,R_{\odot}$[59]). We identify no variability that could be attributed to this contaminating source, therefore we assume it to be constant, and that light curve amplitude has been correctly corrected by the SPOC pipeline.

Optical spectra were obtained at the Palomar 200-inch telescope with DBSP using a low resolution mode ($R \simeq 1200$). We obtained 40 exposures of 120 seconds covering 1.65 hours on March 02 2020. Both blue and red arms were reduced with a custom PYRAF pipeline[60], which performs bias subtraction, flat-field correction, wavelength calibration, optimal spectral extraction, and flux calibration. The trailed spectra are shown in Supplementary Fig. 7, and clearly show periodical changes of the line centres. Finally, we obtained ten 60 second exposures with ESI at the Keck II telescope on September 10 2020, which were combined into a $R \simeq 6000$, high signal-to-noise ratio ($S/N \simeq 170$) spectrum.

The spectral fit of the hot subdwarf

The observed spectra were matched to a model grid by χ^2 minimisation[61,62]. The quantitative spectral analysis is based on a new grid of model atmospheres and synthetic hydrogen and helium spectra that account for deviations from local thermodynamic equilibrium (LTE). We start from an LTE temperature/density stratification calculated with the ATLAS12 code[63]. Non-LTE population numbers of hydrogen and helium levels are then calculated with the DETAIL code[64,65] and handed back to ATLAS12 to correct the atmospheric structure for non-LTE effects in an iterative process[66]. After convergence, DETAIL is used again to solve the coupled equations of radiative transfer and statistical equilibrium numerically. Finally the SURFACE code[64,65] is used to calculate the emergent spectrum using the non-LTE occupation numbers and detailed line-broadening tables. Recent updates to all three codes[66] such as the implementation of the occupation probability formalism[67] for hydrogen, and Stark broadening tables for hydrogen and neutral helium[68,69] are considered. We first fitted the co-added DBSP spectrum, which has better normalisation and covers the Balmer jump, to determine T_{eff} and $\log g$. We find $T_{\mathrm{eff}} = 33640 \pm 640$ K and $\log g = 5.54 \pm 0.06$. Next we fit the higher-resolution ESI spectrum to determine $v \sin i$ and $\log y$, fixing the values of T_{eff} and $\log g$ to those determined from the DBSP spectrum. We fit only the helium lines, which are more sensitive than the Balmer lines, obtaining $\log y = -1.57 \pm 0.14$ and $v \sin i = 152 \pm 7$ km s^{-1}.

The SED fitting method

The observed magnitudes were matched to a synthetic flux distribution employing a χ^2 based fitting routine[70]. The synthetic flux distribution is interpolated from a grid of model SEDs calculated with ATLAS12, as described in the previous section, for

---

[1] The pixel size of TESS is 21".

the spectroscopically inferred atmospheric parameters. With the SED fit, we derive the angular diameter $\Theta = 2R/d$ (with the stellar radius R and distance d), a scaling factor derived from the observed flux $f(\lambda)$ and the synthetic stellar surface flux $F(\lambda)$ by making use of the geometric flux dilution, that is, $f(\lambda) = \Theta^2 F(\lambda)/4$. The radius can then be determined from $R = \Theta/(2\varpi)$ using the trigonometric parallax measurement ϖ provided by the second data release of *Gaia*, which has high-precision and quality indicators within specifications, in particular the re-normalised unit weight error[71] (RUWE).

As HD 265435 is located at low Galactic latitude ($b = +14.8°$), interstellar reddening must be taken into account by fitting the interstellar colour excess along with the angular diameter. To model interstellar absorption we use the reddening law of Fitzpatrick et al.[72]. We find interstellar reddening to be relatively small, with E(B-V)= 0.041 ± 0.011, compared to values from reddening maps[73,74], implying that most of the line-of-sight reddening occurs beyond HD 265435. We derive the stellar radius from the angular diameter Θ and the parallax ϖ by accounting for the *Gaia* DR2 zero point offset of -0.029 mas[75], and find $R = 0.204 \pm 0.007\ R_\odot$. Our fit is shown in Supplementary Fig. 8.

The radial-velocity fitting method

Radial velocities were determined using the `iraf` package `rvsao`[76] by performing cross-correlation with the task `xcsao`. Barycentric corrections were calculated and applied within this same task. We initially used a spectral template for a pure-hydrogen atmosphere with $T_{\rm eff} = 30\,000$ K and $\log\ g = 5.5$. Each spectrum was then Doppler-corrected, and all spectra from the same arm were co-added. The co-added spectrum was used as input for the spectral fit. A template calculated using the best parameters from the spectroscopic fit was then used to re-calculate the radial velocities with `xcsao`. The values obtained (given in Supplementary Tables 3 and 4) were consistent with the initial values using the pure-hydrogen template, but uncertainties were lower by a factor of two. We performed a fit to the radial velocity curve using the Markov-chain Monte Carlo method (MCMC) implemented with the `emcee` package[77] in order to obtain realistic uncertainties. We assume a circular orbit, and thus fit the radial velocities using:

$$RV(t) \quad = \quad V_0 + K_{\rm sdB} \sin[2\pi(t - t_0)/P], \tag{3}$$

where V_0 is the systemic velocity, $K_{\rm sdB}$ is the radial velocity semi-amplitude of the sdB, t_0 is the zero point of the ephemeris, and P is the orbital period. The period was fixed to the photometric period, whereas t_0 was allowed to vary P/2. The velocities V_0 and $K_{\rm sdB}$ were left to vary freely within physical limits, but we used values from χ^2 minimisation as the initial guess. We obtained $V_0 = 8 \pm 5$ km s^{-1} and $K_{\rm sdB} = 342 \pm 7$ km s^{-1}.

The Galactic orbit of HD 265435

We calculated the Galactic orbit of HD 265435 using the package `galpy`[78]. The Galactic potential was modelled with three components (bulge, disk, and halo) plus a central black hole of mass $4 \times 10^6 M_\odot$[78,79]. The Sun was placed at a distance of $R_0 = 8.27 \pm 0.29$ kpc from the Galactic centre with peculiar motion in the Local Standard of Rest of $(U_\odot, V_\odot, W_\odot) = (11.1, 12.24, 7.25)$ km s^{-1}, and the Milky way rotation speed at the Solar circle was set to $V_c = 238 \pm 9$ km s^{-1}[80,81]. The system shows dynamics consistent with the thin disk of the Galaxy, as can be seen in Supplementary Fig. 9. Other indicators, namely the Galactic velocity components (U, V, W), and angular momementum and eccentricity (J_z and e), also point to thin disk membership.

The light-curve fitting method

We used LCURVE[35] to carry out the light curve analysis. This code uses a grid of points to model the two stars, with shapes set by a Roche potential. The flux emitted by each grid point is calculated from a blackbody with a given estimated temperature at the bandpass wavelength, taking into account corrections for limb darkening, gravity darkening, Doppler beaming, and reflection effects.

We assume that the orbit is circular, as done for the radial velocity fit. The temperature of the hot subdwarf was fixed at the value determined from the spectroscopy. The lack of blue-excess in the SED fit implies a maximum temperature for the companion of $T_{\rm comp} \approx 90\,000$ K. Assuming the minimum mass obtained from the spectroscopy and the mass-radius relationship for a carbon-oxygen white dwarf (which will give the maximum radius, and therefore maximum luminosity, for the unseen companion), we obtain that the companion contribution to the light is no more than 0.5%. Test-runs of an MCMC fit to the light curve showed that the companion temperature and radius indeed cannot be constrained given the lack of contribution to the observed flux. Therefore we kept the companion temperature and radius fixed to arbitrary values of $T_{\rm comp} = 30\,000$ K and $R_{\rm comp} = 0.02\ R_\odot$, which are consistent with a white dwarf and result in a contribution of $\sim 0.15\%$.

For the hot subdwarf, limb-darkening and gravity darkening coefficients, as well as the Doppler boosting factor, were interpolated from the tables 4 and y of Claret et al.[82]. We used the values for a pure-hydrogen composition ($\log[H/He] = -10.0$), because coefficients are unavailable at our derived values of $T_{\rm eff}$ and $\log\ g$ for models with intermediate helium abundance. Test-runs indicate that this choice does not affect our solution significantly, and leaving these parameters as free results in values consistent with the tabulated values that were use. These coefficients were all set to zero for the secondary, as it has no measurable contribution. This leaves as free parameters in our light curve fit the mass ratio q, the inclination angle i, the scaled radius of the primary $r_{\rm sdB} = R_{\rm sdB}/a$, where a is the orbital distance, and the velocity scale, $V_{\rm scale} = (K_{\rm sdB} + K_{\rm comp})/\sin\ i$.

We first computed a preliminary fit of the light curve phased to the period determined from the Lomb-Scargle periodogram using the Levenberg–Marquardt algorithm for χ^2 minimisation. For this initial fit our goal was not to obtain the best physical solution, but to calculate a model describing the light curve well enough to allow a more precise determination of the ephemeris, and to subtract the binary contribution from the light curve in order to determine the contribution of pulsations. The pulsation analysis was carried out with PERIOD04[83]. We found 33 frequencies above a detection level of five times the average amplitude of the Fourier transform. We performed a global fit in PERIOD04 using all 33 identified frequencies, and subtracted the obtained model from the original light curve.

Next we performed a MCMC fit to the pulsations-subtracted light curve phase-folded to the determined period. We applied a Gaussian prior to the log g of the primary using the value and uncertainty determined with the spectroscopy fit, as well as a Gaussian prior to the inclination given the inclination derived from our measured values of $v \sin i$, radius and rotation period, which is equal to the orbital period. A third Gaussian prior was used on the radial velocity semi-amplitude of the hot subdwarf, to guarantee its consistency with the value estimated from spectroscopic observations. We ran 200 walkers for 5000 trials and discarded the first 1000 trials as burn-in. Our best-fit model is shown in the top panel of Fig. 2, and the corner plot for our MCMC run is shown in Suppementary Fig. 10.

The evolution of the system

We conducted a numerical analysis of this system using the Modules for Experiments in Stellar Astrophysics (MESA) release 12778[84–88]. We note that the radius of the sdB component radius is about 1.7 times that of a pure helium sdB of the same mass[37], which hints at the presence of a thin ($\sim 0.001\,{\rm M}_\odot$) remnant hydrogen-rich envelope[38]. We found that the observational parameters best fit an evolved helium star with a remnant hydrogen envelope of $0.001\,{\rm M}_\odot$ and solar metallicity. This model was placed in a binary system with an orbital period of $P_{\rm orb} = 100\,{\rm min}$ and a $1.03\,{\rm M}_\odot$ white dwarf, approximated as a point mass.

We include the effects of rotation, assuming tidal locking, angular momentum loss through gravitational radiation and a nominal wind following a prescription by Jager et al. 1998[89], while RLOF-driven mass transfer is assumed to be conservative. Preceding any interaction, the system is expected to lose angular momentum through the emission of gravitational radiation, leading to RLOF after $\sim 23\,{\rm Myr}$. For the following $\sim 10\,{\rm Myr}$ of this RLOF phase, the transferred material will be hydrogen enriched with mass transfer rates well below $10^{-9}\,{\rm M}_\odot\,{\rm yr}^{-1}$. This may be sufficient to lead to a series of classical nova outbursts by the accreting white dwarf[39,40]. The thus formed close double degenerate binary will then merge $\sim 80\,{\rm Myr}$ from the current epoch. With a likely mass ratio $q \approx 0.485$, this system remains below the threshold mass ratio of $q_{crit} = 0.63$ above which the donor star must always be dynamically disrupted once RLOF occurs[90], but given the masses of the two companions, disruption is still likely. Although the mass ratio remains below that previously predicted[91,92] for likely progenitor systems of typical SN Ia, of $q \approx 0.9$, a thermonuclear supernova is the most likely outcome, given the high total mass of the system, although the observed spectrum is not likely to resemble a typical SN Ia, but may instead resemble a SN Iax[93,94] or an otherwise spectrally peculiar Ia.

An alternative (though less likely) explanation of the large radius of the sdB, as compared with a pure helium star, may be a result of the sdB contracting following the most recent CE phase with a less massive to nonexistent H-envelope. About $0.08\,{\rm M}_\odot$ of helium would be supplied to the accreting white dwarf at mass transfer rates of $3 \times 10^{-8}\,{\rm M}_\odot\,{\rm yr}^{-1}$ following the sdB exhausting its core-He supply, which is sufficiently low to allow for quiescent accumulation of the helium enriched material[44]. Subsequent mass transfer will then strip the sdB of its remaining helium envelope, resulting in one or more non-destructive helium ignitions on the accretor[45], leaving the system as a close white dwarf binary consisting of one low mass $\sim 0.35\,{\rm M}_\odot$ CO white dwarf, and one more massive $\sim 1.05\,{\rm M}_\odot$ CO white dwarf with a $\sim 0.05\,{\rm M}_\odot$ He-envelope.

A number of viable channels for the production of a binaries like HD 265435 have been proposed in the past[37]. Assuming a "no-frills" evolution of the system, i.e. formation as a binary, no appreciable binary interaction before the formation of the sdB in a CE-phase, we can make an estimate of the delay time of the system. Using once more the MESA framework, we find that the likely progenitor of the sdB is a main sequence star in in the mass range of $4.1 - 4.3\,{\rm M}_\odot$, which, with a white dwarf progenitor of $\sim 6\,{\rm M}_\odot$[95], will determine the evolutionary timescale of the system. This is assuming that the system enters a CE phase immediately when the sdB-progenitor has evolved a He core of the appropriate mass, i.e. $\sim 0.5\,{\rm M}_\odot$, and, concurrently, undergoes helium ignition. Under these condition, the lifetime of the progenitor binary is $\sim 132\,{\rm Myr}$. The system requires an additional $\sim 79\,{\rm Myr}$ for the sdB to evolve to its currently observed physical properties. Accordingly, the timescale from zero-age main sequence to merger would be on the order of $\sim 296\,{\rm Myr}$.

References

1. Schmidt, B. P. *et al.* The High-Z Supernova Search: Measuring Cosmic Deceleration and Global Curvature of the Universe Using Type IA Supernovae. *Astrophys. J.* **507**, 46–63, DOI: 10.1086/306308 (1998). astro-ph/9805200.
2. Riess, A. G. *et al.* Observational Evidence from Supernovae for an Accelerating Universe and a Cosmological Constant. *Astron. J.* **116**, 1009–1038, DOI: 10.1086/300499 (1998). astro-ph/9805201.
3. Perlmutter, S. *et al.* Measurements of Ω and Λ from 42 High-Redshift Supernovae. *Astrophys. J.* **517**, 565–586, DOI: 10.1086/307221 (1999). astro-ph/9812133.
4. Riess, A. G., Casertano, S., Yuan, W., Macri, L. M. & Scolnic, D. Large Magellanic Cloud Cepheid Standards Provide a 1% Foundation for the Determination of the Hubble Constant and Stronger Evidence for Physics beyond ΛCDM. *Astrophys. J.* **876**, 85, DOI: 10.3847/1538-4357/ab1422 (2019). 1903.07603.
5. Planck Collaboration *et al.* Planck 2018 results. VI. Cosmological parameters. *arXiv e-prints* arXiv:1807.06209 (2018). 1807.06209.
6. Bernal, J. L., Verde, L. & Riess, A. G. The trouble with H_0. *J. Cosmol. Astropart. Phys.* **2016**, 019, DOI: 10.1088/1475-7516/2016/10/019 (2016). 1607.05617.
7. Hoyle, F. & Fowler, W. A. Nucleosynthesis in Supernovae. *Astrophys. J.* **132**, 565, DOI: 10.1086/146963 (1960).
8. Chandrasekhar, S. The Maximum Mass of Ideal White Dwarfs. *Astrophys. J.* **74**, 81, DOI: 10.1086/143324 (1931).
9. Hillebrandt, W., Kromer, M., Röpke, F. K. & Ruiter, A. J. Towards an understanding of Type Ia supernovae from a synthesis of theory and observations. *Front. Phys.* **8**, 116–143, DOI: 10.1007/s11467-013-0303-2 (2013). 1302.6420.
10. Whelan, J. & Iben, J., Icko. Binaries and Supernovae of Type I. *Astrophys. J.* **186**, 1007–1014, DOI: 10.1086/152565 (1973).
11. Iben, J., I. & Tutukov, A. V. Supernovae of type I as end products of the evolution of binaries with components of moderate initial mass. *Astrophys. J. Suppl.* **54**, 335–372, DOI: 10.1086/190932 (1984).
12. Liu, D., Wang, B. & Han, Z. The double-degenerate model for the progenitors of Type Ia supernovae. *Mon. Not. R. Astron. Soc.* **473**, 5352–5361, DOI: 10.1093/mnras/stx2756 (2018). 1710.03961.
13. Han, Z. & Podsiadlowski, P. The single-degenerate channel for the progenitors of Type Ia supernovae. *Mon. Not. R. Astron. Soc.* **350**, 1301–1309, DOI: 10.1111/j.1365-2966.2004.07713.x (2004). astro-ph/0309618.
14. Rebassa-Mansergas, A., Toonen, S., Korol, V. & Torres, S. Where are the double-degenerate progenitors of Type Ia supernovae? *Mon. Not. R. Astron. Soc.* **482**, 3656–3668, DOI: 10.1093/mnras/sty2965 (2019). 1809.07158.
15. Maoz, D. & Mannucci, F. Type-Ia Supernova Rates and the Progenitor Problem: A Review. *Publ. Astron. Soc. Aust.* **29**, 447–465, DOI: 10.1071/AS11052 (2012). 1111.4492.
16. Santander-García, M. *et al.* The double-degenerate, super-Chandrasekhar nucleus of the planetary nebula Henize 2-428. *Nature* **519**, 63–65, DOI: 10.1038/nature14124 (2015). 1609.00178.
17. Reindl, N. *et al.* An in-depth reanalysis of the alleged type Ia supernova progenitor Henize 2-428. *Astron. Astrophys.* **638**, A93, DOI: 10.1051/0004-6361/202038117 (2020). 2006.14688.
18. Napiwotzki, R. *et al.* The ESO supernovae type Ia progenitor survey (SPY). The radial velocities of 643 DA white dwarfs. *Astron. Astrophys.* **638**, A131, DOI: 10.1051/0004-6361/201629648 (2020). 1906.10977.
19. Maxted, P. F. L., Marsh, T. R. & North, R. C. KPD 1930+2752: a candidate Type Ia supernova progenitor. *Mon. Not. R. Astron. Soc.* **317**, L41–L44, DOI: 10.1046/j.1365-8711.2000.03856.x (2000). astro-ph/0007257.
20. Geier, S. *et al.* The hot subdwarf B + white dwarf binary KPD 1930+2752. A supernova type Ia progenitor candidate. *Astron. Astrophys.* **464**, 299–307, DOI: 10.1051/0004-6361:20066098 (2007). astro-ph/0609742.
21. Vennes, S., Kawka, A., O'Toole, S. J., Németh, P. & Burton, D. The Shortest Period sdB Plus White Dwarf Binary CD-30 11223 (GALEX J1411-3053). *Astrophys. J. Lett.* **759**, L25, DOI: 10.1088/2041-8205/759/1/L25 (2012). 1210.1512.
22. Geier, S. *et al.* A progenitor binary and an ejected mass donor remnant of faint type Ia supernovae. *Astron. Astrophys.* **554**, A54, DOI: 10.1051/0004-6361/201321395 (2013). 1304.4452.
23. Amaro-Seoane, P. *et al.* Laser Interferometer Space Antenna. *arXiv e-prints* arXiv:1702.00786 (2017). 1702.00786.
24. Ricker, G. R. *et al.* Transiting Exoplanet Survey Satellite (TESS). *J. Astron. Telesc. Instruments, Syst.* **1**, 014003, DOI: 10.1117/1.JATIS.1.1.014003 (2015).

25. Oke, J. B. & Gunn, J. E. An Efficient Low Resolution and Moderate Resolution Spectrograph for the Hale Telescope. *Publ. Astron. Soc. Pac.* **94**, 586, DOI: 10.1086/131027 (1982).

26. Gaia Collaboration. VizieR Online Data Catalog: Gaia DR2 (Gaia Collaboration, 2018). *VizieR Online Data Catalog* I/345 (2018).

27. Høg, E. *et al.* The Tycho-2 catalogue of the 2.5 million brightest stars. *Astron. Astrophys.* **355**, L27–L30 (2000).

28. Lomb, N. R. Least-Squares Frequency Analysis of Unequally Spaced Data. *Astrophys. Space Sci.* **39**, 447–462, DOI: 10.1007/BF00648343 (1976).

29. Scargle, J. D. Studies in astronomical time series analysis. II. Statistical aspects of spectral analysis of unevenly spaced data. *Astrophys. J.* **263**, 835–853, DOI: 10.1086/160554 (1982).

30. Shakura, N. I. & Postnov, K. A. Doppler-effect modulation of the observed radiation flux from ultracompact binary stars. *Astron. Astrophys.* **183**, L21–L22 (1987).

31. Charpinet, S., Fontaine, G., Brassard, P. & Dorman, B. The Potential of Asteroseismology for Hot, Subdwarf B Stars: A New Class of Pulsating Stars? *Astrophys. J. Lett.* **471**, L103, DOI: 10.1086/310335 (1996). astro-ph/9606069.

32. Kilkenny, D., Koen, C., O'Donoghue, D. & Stobie, R. S. A new class of rapidly pulsating star - I. EC 14026-2647, the class prototype. *Mon. Not. R. Astron. Soc.* **285**, 640–644, DOI: 10.1093/mnras/285.3.640 (1997).

33. Geier, S., Karl, C., Edelmann, H., Heber, U. & Napiwotzki, R. Binary sdB Stars with Massive Compact Companions. In Heber, U., Jeffery, C. S. & Napiwotzki, R. (eds.) *Hot Subdwarf Stars and Related Objects*, vol. 392 of *Astronomical Society of the Pacific Conference Series*, 207 (2008).

34. Geier, S., Raddi, R., Gentile Fusillo, N. P. & Marsh, T. R. The population of hot subdwarf stars studied with Gaia. II. The Gaia DR2 catalogue of hot subluminous stars. *Astron. Astrophys.* **621**, A38, DOI: 10.1051/0004-6361/201834236 (2019). 1810.09321.

35. Copperwheat, C. M. *et al.* Physical properties of IP Pegasi: an eclipsing dwarf nova with an unusually cool white dwarf. *Mon. Not. R. Astron. Soc.* **402**, 1824–1840, DOI: 10.1111/j.1365-2966.2009.16010.x (2010). 0911.1637.

36. Lauffer, G. R., Romero, A. D. & Kepler, S. O. New full evolutionary sequences of H- and He-atmosphere massive white dwarf stars using MESA. *Mon. Not. R. Astron. Soc.* **480**, 1547–1562, DOI: 10.1093/mnras/sty1925 (2018). 1807.04774.

37. Heber, U. Hot Subluminous Stars. *Publ. Astron. Soc. Pac.* **128**, 082001, DOI: 10.1088/1538-3873/128/966/082001 (2016). 1604.07749.

38. Preece, H. P., Jeffery, C. S. & Tout, C. A. Asteroseismology of tidally distorted sdB stars. *Mon. Not. R. Astron. Soc.* **489**, 3066–3072, DOI: 10.1093/mnras/stz2292 (2019).

39. Iben, J., Icko, Fujimoto, M. Y. & MacDonald, J. On Mass-Transfer Rates in Classical Nova Precursors. *Astrophys. J.* **384**, 580, DOI: 10.1086/170900 (1992).

40. Shara, M. M., Prialnik, D., Hillman, Y. & Kovetz, A. The Masses and Accretion Rates of White Dwarfs in Classical and Recurrent Novae. *Astrophys. J.* **860**, 110, DOI: 10.3847/1538-4357/aabfbd (2018). 1804.06880.

41. Nomoto, K. Supernova explosions in accreting whiteddwarfs and Type I supernovae. In Wheeler, J. C. (ed.) *Texas Workshop on Type I Supernovae*, 164–181 (1980).

42. Livne, E. Successive Detonations in Accreting White Dwarfs as an Alternative Mechanism for Type I Supernovae. *Astrophys. J. Lett.* **354**, L53, DOI: 10.1086/185721 (1990).

43. Shen, K. J. & Bildsten, L. The Ignition of Carbon Detonations via Converging Shock Waves in White Dwarfs. *Astrophys. J.* **785**, 61, DOI: 10.1088/0004-637X/785/1/61 (2014). 1305.6925.

44. Woosley, S. E. & Kasen, D. Sub-Chandrasekhar Mass Models for Supernovae. *Astrophys. J.* **734**, 38, DOI: 10.1088/0004-637X/734/1/38 (2011). 1010.5292.

45. Neunteufel, P., Yoon, S. C. & Langer, N. Models for the evolution of close binaries with He-star and white dwarf components towards Type Ia supernova explosions. *Astron. Astrophys.* **589**, A43, DOI: 10.1051/0004-6361/201527845 (2016). 1603.00768.

46. Kraft, R. P., Mathews, J. & Greenstein, J. L. Binary Stars among Cataclysmic Variables. II. Nova WZ Sagittae: a Possible Radiator of Gravitational Waves. *Astrophys. J.* **136**, 312–315, DOI: 10.1086/147381 (1962).

47. Shah, S., van der Sluys, M. & Nelemans, G. Using electromagnetic observations to aid gravitational-wave parameter estimation of compact binaries observed with LISA. *Astron. Astrophys.* **544**, A153, DOI: 10.1051/0004-6361/201219309 (2012). 1207.6770.

48. Moore, C. J., Cole, R. H. & Berry, C. P. L. Gravitational-wave sensitivity curves. *Class. Quantum Gravity* **32**, 015014, DOI: 10.1088/0264-9381/32/1/015014 (2015). 1408.0740.

49. Robson, T., Cornish, N. J. & Liu, C. The construction and use of LISA sensitivity curves. *Class. Quantum Gravity* **36**, 105011, DOI: 10.1088/1361-6382/ab1101 (2019). 1803.01944.

50. Kupfer, T. *et al.* LISA verification binaries with updated distances from Gaia Data Release 2. *Mon. Not. R. Astron. Soc.* **480**, 302–309, DOI: 10.1093/mnras/sty1545 (2018). 1805.00482.

51. Neunteufel, P., Yoon, S. C. & Langer, N. Evolution of helium star plus carbon-oxygen white dwarf binary systems and implications for diverse stellar transients and hypervelocity stars. *Astron. Astrophys.* **627**, A14, DOI: 10.1051/0004-6361/201935322 (2019). 1904.12421.

52. Kupfer, T. *et al.* The First Ultracompact Roche Lobe-Filling Hot Subdwarf Binary. *Astrophys. J.* **891**, 45, DOI: 10.3847/1538-4357/ab72ff (2020). 2002.01485.

53. Kupfer, T. *et al.* A New Class of Roche Lobe-filling Hot Subdwarf Binaries. *Astrophys. J. Lett.* **898**, L25, DOI: 10.3847/2041-8213/aba3c2 (2020). 2007.05349.

54. Jurić, M. *et al.* The Milky Way Tomography with SDSS. I. Stellar Number Density Distribution. *Astrophys. J.* **673**, 864–914, DOI: 10.1086/523619 (2008). astro-ph/0510520.

55. Han, Z., Podsiadlowski, P., Maxted, P. F. L. & Marsh, T. R. The origin of subdwarf B stars - II. *Mon. Not. R. Astron. Soc.* **341**, 669–691, DOI: 10.1046/j.1365-8711.2003.06451.x (2003). astro-ph/0301380.

56. Wang, B. *et al.* Birthrates and delay times of Type Ia supernovae. *Sci. China Physics, Mech. Astron.* **53**, 586–590, DOI: 10.1007/s11433-010-0152-8 (2010). 1002.4229.

57. Li, W. *et al.* Nearby supernova rates from the Lick Observatory Supernova Search - III. The rate-size relation, and the rates as a function of galaxy Hubble type and colour. *Mon. Not. R. Astron. Soc.* **412**, 1473–1507, DOI: 10.1111/j.1365-2966.2011.18162.x (2011). 1006.4613.

58. Maoz, D., Mannucci, F. & Nelemans, G. Observational Clues to the Progenitors of Type Ia Supernovae. *Annu. Rev. Astron. Astrophys.* **52**, 107–170, DOI: 10.1146/annurev-astro-082812-141031 (2014). 1312.0628.

59. Andrae, R. *et al.* Gaia Data Release 2. First stellar parameters from Apsis. *Astron. Astrophys.* **616**, A8, DOI: 10.1051/0004-6361/201732516 (2018). 1804.09374.

60. Bellm, E. C. & Sesar, B. pyraf-dbsp: Reduction pipeline for the Palomar Double Beam Spectrograph (2016). 1602.002.

61. Saffer, R. A., Bergeron, P., Koester, D. & Liebert, J. Atmospheric Parameters of Field Subdwarf B Stars. *Astrophys. J.* **432**, 351, DOI: 10.1086/174573 (1994).

62. Napiwotzki, R., Green, P. J. & Saffer, R. A. A Comparative Study of the Mass Distribution of Extreme-Ultraviolet-selected White Dwarfs. *Astrophys. J.* **517**, 399–415, DOI: 10.1086/307170 (1999). astro-ph/9901027.

63. Kurucz, R. L. Status of the ATLAS 12 Opacity Sampling Program and of New Programs for Rosseland and for Distribution Function Opacity. In Adelman, S. J., Kupka, F. & Weiss, W. W. (eds.) *M.A.S.S., Model Atmospheres and Spectrum Synthesis*, vol. 108 of *Astronomical Society of the Pacific Conference Series*, 160 (1996).

64. Giddings, J. R. Ph.D. thesis, Univ. London (1981).

65. Butler, K. & Giddings, J. R. *Newsl. Analysis Astron. Spectra* **No. 9 (Univ. London)** (1985).

66. Irrgang, A., Kreuzer, S., Heber, U. & Brown, W. A quantitative spectral analysis of 14 hypervelocity stars from the MMT survey. *Astron. Astrophys.* **615**, L5, DOI: 10.1051/0004-6361/201833315 (2018). 1806.08630.

67. Hubeny, I., Hummer, D. G. & Lanz, T. NLTE model stellar atmospheres with line blanketing near the series limits. *Astron. Astrophys.* **282**, 151–167 (1994).

68. Tremblay, P. E. & Bergeron, P. Spectroscopic Analysis of DA White Dwarfs: Stark Broadening of Hydrogen Lines Including Nonideal Effects. *Astrophys. J.* **696**, 1755–1770, DOI: 10.1088/0004-637X/696/2/1755 (2009). 0902.4182.

69. Beauchamp, A., Wesemael, F. & Bergeron, P. Spectroscopic Studies of DB White Dwarfs: Improved Stark Profiles for Optical Transitions of Neutral Helium. *Astrophys. J. Suppl.* **108**, 559–573, DOI: 10.1086/312961 (1997).

70. Heber, U., Irrgang, A. & Schaffenroth, J. Spectral energy distributions and colours of hot subluminous stars. *Open Astron.* **27**, 35–43, DOI: 10.1515/astro-2018-0008 (2018). 1712.06546.

71. Lindegren, L. Re-normalising the astrometric chi-square in Gaia DR2, GAIA-C3-TN-LU-LL-124,. *Re-normalising astrometric chi-square Gaia DR2, GAIA-C3-TN-LU-LL-124* **www.rssd.esa.int/doc_fetch.php?id=3757412** (2018).

72. Fitzpatrick, E. L., Massa, D., Gordon, K. D., Bohlin, R. & Clayton, G. C. An Analysis of the Shapes of Interstellar Extinction Curves. VII. Milky Way Spectrophotometric Optical-through-ultraviolet Extinction and Its R-dependence. *Astrophys. J.* **886**, 108, DOI: 10.3847/1538-4357/ab4c3a (2019). 1910.08852.

73. Schlegel, D. J., Finkbeiner, D. P. & Davis, M. Maps of Dust Infrared Emission for Use in Estimation of Reddening and Cosmic Microwave Background Radiation Foregrounds. *Astrophys. J.* **500**, 525–553, DOI: 10.1086/305772 (1998). astro-ph/9710327.

74. Schlafly, E. F. & Finkbeiner, D. P. Measuring Reddening with Sloan Digital Sky Survey Stellar Spectra and Recalibrating SFD. *Astrophys. J.* **737**, 103, DOI: 10.1088/0004-637X/737/2/103 (2011). 1012.4804.

75. Lindegren, L. *et al.* Gaia Data Release 2. The astrometric solution. *Astron. Astrophys.* **616**, A2, DOI: 10.1051/0004-6361/201832727 (2018). 1804.09366.

76. Kurtz, M. J. & Mink, D. J. RVSAO 2.0: Digital Redshifts and Radial Velocities. *Publ. Astron. Soc. Pac.* **110**, 934–977, DOI: 10.1086/316207 (1998). astro-ph/9803252.

77. Foreman-Mackey, D., Hogg, D. W., Lang, D. & Goodman, J. emcee: The MCMC Hammer. *Publ. Astron. Soc. Pac.* **125**, 306, DOI: 10.1086/670067 (2013). 1202.3665.

78. Bovy, J. galpy: A python Library for Galactic Dynamics. *Astrophys. J. Suppl.* **216**, 29, DOI: 10.1088/0067-0049/216/2/29 (2015). 1412.3451.

79. Bovy, J. & Rix, H.-W. A Direct Dynamical Measurement of the Milky Way's Disk Surface Density Profile, Disk Scale Length, and Dark Matter Profile at 4 kpc <~R <~9 kpc. *Astrophys. J.* **779**, 115, DOI: 10.1088/0004-637X/779/2/115 (2013). 1309.0809.

80. Schönrich, R., Binney, J. & Dehnen, W. Local kinematics and the local standard of rest. *Mon. Not. R. Astron. Soc.* **403**, 1829–1833, DOI: 10.1111/j.1365-2966.2010.16253.x (2010). 0912.3693.

81. Schönrich, R. Galactic rotation and solar motion from stellar kinematics. *Mon. Not. R. Astron. Soc.* **427**, 274–287, DOI: 10.1111/j.1365-2966.2012.21631.x (2012). 1207.3079.

82. Claret, A. *et al.* Gravity and limb-darkening coefficients for compact stars: DA, DB, and DBA eclipsing white dwarfs. *Astron. Astrophys.* **634**, A93, DOI: 10.1051/0004-6361/201937326 (2020). 2001.07129.

83. Lenz, P. & Breger, M. Period04: Statistical analysis of large astronomical time series (2014). 1407.009.

84. Paxton, B. *et al.* Modules for Experiments in Stellar Astrophysics (MESA). *Astrophys. J. Suppl.* **192**, 3, DOI: 10.1088/0067-0049/192/1/3 (2011). 1009.1622.

85. Paxton, B. *et al.* Modules for Experiments in Stellar Astrophysics (MESA): Planets, Oscillations, Rotation, and Massive Stars. *Astrophys. J. Suppl.* **208**, 4, DOI: 10.1088/0067-0049/208/1/4 (2013). 1301.0319.

86. Paxton, B. *et al.* Modules for Experiments in Stellar Astrophysics (MESA): Binaries, Pulsations, and Explosions. *Astrophys. J. Suppl.* **220**, 15, DOI: 10.1088/0067-0049/220/1/15 (2015). 1506.03146.

87. Paxton, B. *et al.* Modules for Experiments in Stellar Astrophysics (MESA): Convective Boundaries, Element Diffusion, and Massive Star Explosions. *Astrophys. J. Suppl.* **234**, 34, DOI: 10.3847/1538-4365/aaa5a8 (2018). 1710.08424.

88. Paxton, B. *et al.* Modules for Experiments in Stellar Astrophysics (MESA): Pulsating Variable Stars, Rotation, Convective Boundaries, and Energy Conservation. *Astrophys. J. Suppl.* **243**, 10, DOI: 10.3847/1538-4365/ab2241 (2019). 1903.01426.

89. de Jager, C., Nieuwenhuijzen, H. & van der Hucht, K. A. Mass loss rates in the Hertzsprung-Russell diagram. *Astron. Astrophys. Suppl. Ser.* **72**, 259–289 (1988).

90. Eggleton, P. *Evolutionary Processes in Binary and Multiple Stars* (2006).

91. Pakmor, R., Hachinger, S., Röpke, F. K. & Hillebrand t, W. Violent mergers of nearly equal-mass white dwarf as progenitors of subluminous Type Ia supernovae. *Astron. Astrophys.* **528**, A117, DOI: 10.1051/0004-6361/201015653 (2011). 1102.1354.

92. Sato, Y. *et al.* The Critical Mass Ratio of Double White Dwarf Binaries for Violent Merger-induced Type Ia Supernova Explosions. *Astrophys. J.* **821**, 67, DOI: 10.3847/0004-637X/821/1/67 (2016). 1603.01088.

93. Foley, R. J. *et al.* Type Iax Supernovae: A New Class of Stellar Explosion. *Astrophys. J.* **767**, 57, DOI: 10.1088/0004-637X/767/1/57 (2013). 1212.2209.

94. Wang, B., Justham, S. & Han, Z. Producing Type Iax supernovae from a specific class of helium-ignited WD explosions. *Astron. Astrophys.* **559**, A94, DOI: 10.1051/0004-6361/201322298 (2013). 1310.2297.

95. Weidemann, V. Revision of the initial-to-final mass relation. *Astron. Astrophys.* **363**, 647–656 (2000).

96. Astropy Collaboration *et al.* Astropy: A community Python package for astronomy. *Astron. Astrophys.* **558**, A33, DOI: 10.1051/0004-6361/201322068 (2013). 1307.6212.

97. Price-Whelan, A. M. *et al.* The Astropy Project: Building an Open-science Project and Status of the v2.0 Core Package. *Astron. J.* **156**, 123, DOI: 10.3847/1538-3881/aabc4f (2018).

98. Henden, A. A., Levine, S., Terrell, D. & Welch, D. L. APASS - The Latest Data Release. In *American Astronomical Society Meeting Abstracts #225*, vol. 225 of *American Astronomical Society Meeting Abstracts*, 336.16 (2015).

99. Chambers, K. C. *et al.* VizieR Online Data Catalog: The Pan-STARRS release 1 (PS1) Survey - DR1 (Chambers+, 2016). *VizieR Online Data Catalog* **2349** (2017).

100. Skrutskie, M. F. *et al.* The Two Micron All Sky Survey (2MASS). *Astron. J.* **131**, 1163–1183, DOI: 10.1086/498708 (2006).

101. Evans, D. W. *et al.* Gaia Data Release 2. Photometric content and validation. *Astron. Astrophys.* **616**, A4, DOI: 10.1051/0004-6361/201832756 (2018). 1804.09368.

102. Maíz Apellániz, J. & Weiler, M. Reanalysis of the Gaia Data Release 2 photometric sensitivity curves using HST/STIS spectrophotometry. *Astron. Astrophys.* **619**, A180, DOI: 10.1051/0004-6361/201834051 (2018). 1808.02820.

103. Cutri, R. M. & et al. VizieR Online Data Catalog: AllWISE Data Release (Cutri+ 2013). *VizieR Online Data Catalog* II/328 (2014).

104. Schlafly, E. F., Meisner, A. M. & Green, G. M. The unWISE Catalog: Two Billion Infrared Sources from Five Years of WISE Imaging. *Astrophys. J. Suppl.* **240**, 30, DOI: 10.3847/1538-4365/aafbea (2019). 1901.03337.

105. Foreman-Mackey, D. corner.py: Scatterplot matrices in python. *The J. Open Source Softw.* **1**, 24, DOI: 10.21105/joss.00024 (2016).

Acknowledgements

IP was partially funded by the Deutsche Forschungsgemeinschaft under grant GE2506/12-1. DS was supported by the Deutsche Forschungsgemeinschaft (DFG) under grant HE 1356/70-1. BB acknowledges support from NASA under TESS Guest Investigator program grant 80NSSC19K1720. We thank Tom Marsh for providing an MCMC wrapper to be used with LCURVE.

This research made extensive use of Astropy,[2] a community-developed core Python package for Astronomy[96,97]

This paper includes data collected by the TESS mission. Funding for the TESS mission is provided by the NASA Explorer Program.

This work has made use of data from the European Space Agency (ESA) mission *Gaia* (`https://www.cosmos.esa.int/gaia`), processed by the *Gaia* Data Processing and Analysis Consortium (DPAC, `https://www.cosmos.esa.int/web/gaia/dpac/consortium`). Funding for the DPAC has been provided by national institutions, in particular the institutions participating in the *Gaia* Multilateral Agreement.

Author contributions

All authors contributed to the work presented in this paper. IP carried out the radial velocity estimates and fitting, the light curve fitting, and led the writing of the manuscript. SG performed the spectral fitting. PN calculated the evolution of the system. TK did the spectroscopic reduction and cross-checked the light curve fitting. DS and UH performed the SED fitting. AI calculated the spectral models used for SED and spectral fitting. AB calculated the Galactic orbit of the system. JvR performed the spectroscopic observations and contributed to the light curve fit. VS and BNB contributed to the analysis of the light curve. All authors reviewed the manuscript.

Competing interests statement

The authors declare no competing interests.

Supplementary Information

---

[2] http://www.astropy.org

Table 2. Identified p-mode pulsations of the hot subdwarf. The 33 p-mode frequencies above a 5-σ detection level identified and removed from the light curve prior to fitting a binary model. Uncertainties were obtained with 500 Monte Carlo runs in PERIOD04[83] and are given on the last significant digits, e.g. $3371.859(7) = 3371.859 \pm 0.007$.

ID	Frequency (μHz)	Amplitude (ppt)
f1	3371.859(7)	2.34(7)
f2	3035.503(7)	2.23(7)
f3	3203.680(11)	1.45(7)
f4	3050.4(8)	1.25(28)
f5	3219(19)	1.03(39)
f6	3431.656(16)	1.00(7)
f7	3263.410(19)	0.87(7)
f8	2882.22(29)	0.89(8)
f9	3057(27)	0.88(39)
f10	3095(37)	1.1(7)
f11	3540.0(9)	0.86(15)
f12	2926.9(22)	0.84(20)
f13	3387(14)	0.81(34)
f14	3385.7(1.9)	0.78(14)
f15	3049.4(9)	0.75(27)
f16	4127(15)	0.71(31)
f17	3212.832(24)	0.71(7)
f18	2714(37)	0.68(29)
f19	3429.249(23)	0.68(7)
f20	2888(169)	0.65(27)
f21	3225.097(25)	0.65(7)
f22	2867.282(26)	0.63(7)
f23	3668.8(3.2)	0.55(12)
f24	3393(51)	0.51(22)
f25	2759(13)	0.49(16)
f26	3768(22)	0.47(21)
f27	3095(66)	0.63(74)
f28	3779.122(36)	0.42(7)
f29	2881.204(38)	0.43(8)
f30	2720.577(38)	0.41(7)
f31	3261.03(34)	0.41(8)
f32	2208.5(5)	0.39(8)
f33	2544.78(30)	0.38(7)

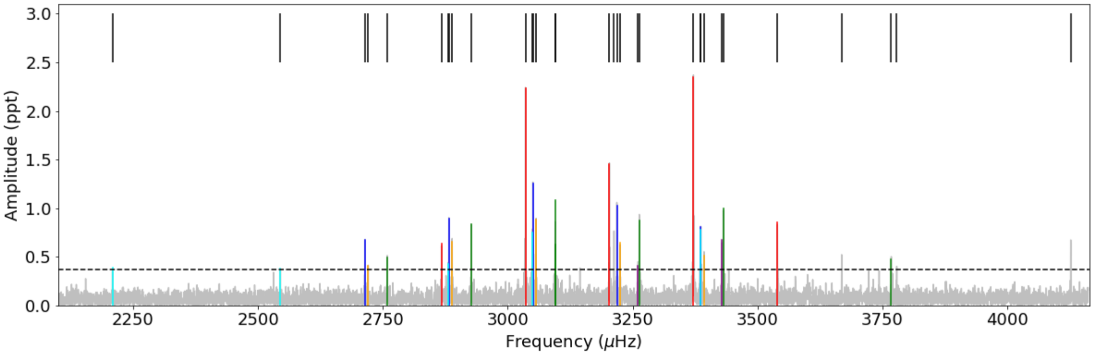

Figure 6. Pulsations of the hot subdwarf. Fourier transform showing the region with identified *p*-modes (marked by the black vertical lines). Modes that are separated by multiples of the orbital period are marked in the same colour. The dashed vertical line was our final detection threshold. Pulsation above the detection limit were subtracted prior to the light curve modelling.

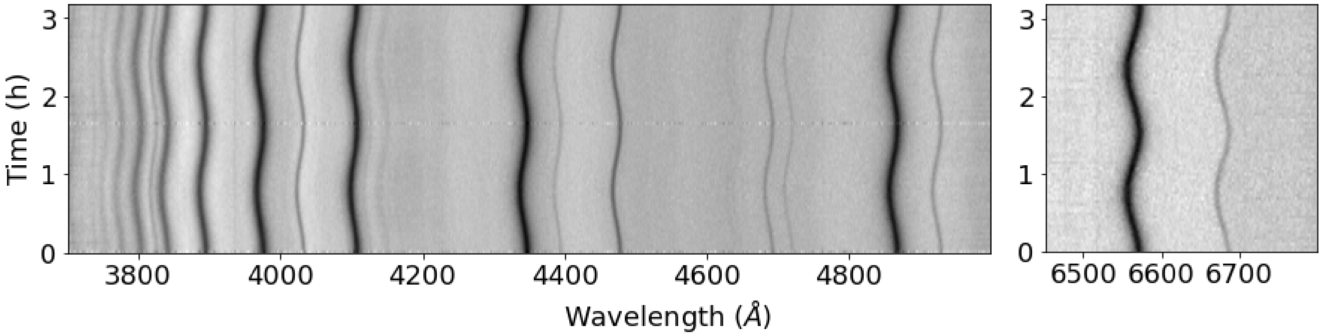

Figure 7. Trailed spectra of the exposures obtained with the Palomar 200-inch telescope. We plot the same spectra twice to cover two cycles and aid visualisation of the radial velocity changes.

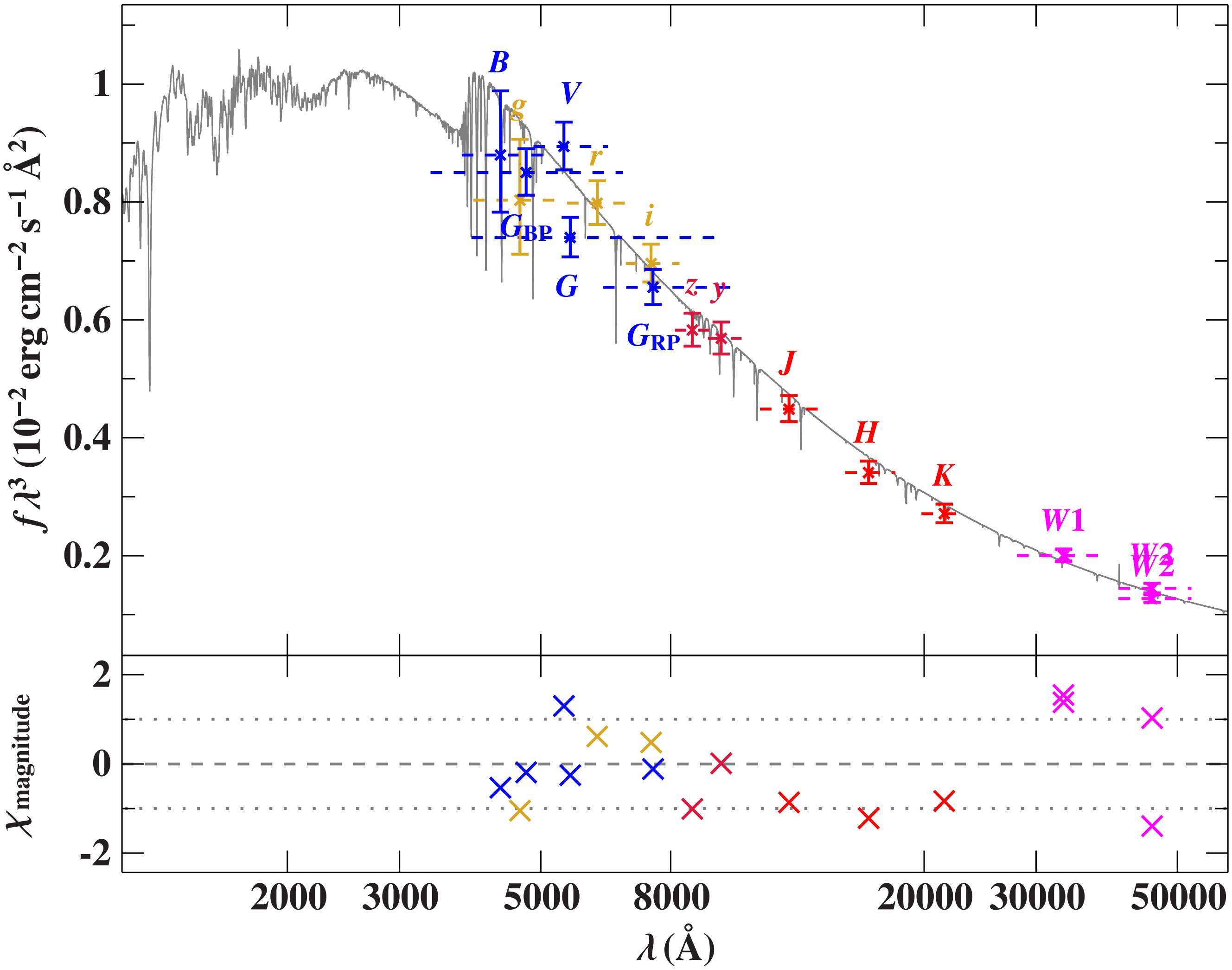

Figure 8. **Comparison of synthetic and observed photometry.** *Top panel:* SED of HD 265435 with filter-averaged fluxes (times wavelength to the power of three) converted from observed magnitudes. The approximate width of the respective filters (widths at 10% of maximum) are shown by dashed lines. The best-fitting model SED, smoothed to a spectral resolution of 6 Å, is shown in grey. *Bottom panel:* Residuals χ, i.e., the difference between synthetic and observed magnitudes divided by the corresponding uncertainties. The different photometric systems are displayed in the following colours: golden for APASS-griz[98], red for PAN-STARRS[99] and 2MASS[100], blue for APASS-Johnson[98] and *Gaia*[101, 102], and magenta for WISE[103, 104].

Table 3. **Radial velocities obtained from spectra taken with the blue channel.**

BJD	RV (km/s)	σ_{RV} (km/s)
2458909.63734	337.03	6.21
2458909.63898	342.66	6.91
2458909.64062	330.93	6.63
2458909.64226	318.61	6.59
2458909.64390	297.84	6.81
2458909.64554	277.98	5.59
2458909.64718	239.58	6.20
2458909.64881	204.68	5.80
2458909.65045	163.12	6.48
2458909.65209	109.46	6.31
2458909.65373	61.75	6.07
2458909.65537	3.07	5.32
2458909.65701	-38.98	5.97
2458909.65865	-87.83	6.45
2458909.66029	-137.82	6.15
2458909.66193	-190.80	5.25
2458909.66357	-225.72	5.70
2458909.66521	-258.85	5.75
2458909.66685	-288.02	6.07
2458909.66849	-307.18	5.90
2458909.67013	-326.84	6.70
2458909.67177	-334.37	6.46
2458909.67341	-335.73	6.89
2458909.67505	-326.83	6.31
2458909.67669	-313.77	6.65
2458909.67833	-293.57	5.47
2458909.67997	-261.68	6.07
2458909.68161	-230.62	5.72
2458909.68325	-189.10	5.74
2458909.68489	-147.20	5.69
2458909.68653	-95.98	5.30
2458909.68817	-50.23	5.56
2458909.68981	5.97	5.83
2458909.69145	49.20	5.99
2458909.69309	107.42	5.66
2458909.69473	149.59	5.75
2458909.69637	198.87	6.33
2458909.69800	236.96	6.15
2458909.69964	280.80	5.81
2458909.70128	306.14	6.61
2458909.70292	329.57	6.62
2458909.70456	343.37	5.99
2458909.70555	348.70	13.38

Table 4. **Radial velocities obtained from spectra taken with the red channel.**

BJD	RV (km/s)	σ_{RV} (km/s)
2458909.63723	370.11	15.86
2458909.63889	398.05	14.45
2458909.64054	390.82	14.35
2458909.64220	342.00	11.94
2458909.64386	319.98	8.81
2458909.64551	288.98	9.11
2458909.64717	257.57	12.85
2458909.64883	238.55	9.51
2458909.65048	165.75	13.11
2458909.65214	126.50	11.93
2458909.65380	60.34	13.94
2458909.65545	8.46	12.71
2458909.65711	-43.24	13.29
2458909.65877	-63.40	14.26
2458909.66042	-115.31	8.95
2458909.66208	-165.17	11.84
2458909.66374	-218.92	11.69
2458909.66539	-251.66	14.47
2458909.66705	-315.21	8.73
2458909.66871	-297.70	18.51
2458909.67036	-352.65	21.30
2458909.67202	-297.57	11.92
2458909.67368	-329.15	23.94
2458909.67533	-298.43	21.41
2458909.67699	-304.48	16.63
2458909.67865	-270.85	11.25
2458909.68030	-256.84	14.66
2458909.68196	-212.91	12.39
2458909.68362	-168.86	12.36
2458909.68527	-114.14	10.04
2458909.68693	-82.01	10.88
2458909.68859	-52.29	11.89
2458909.69024	36.37	8.93
2458909.69190	78.97	10.56
2458909.69355	148.34	13.11
2458909.69521	158.96	12.96
2458909.69687	208.76	10.13
2458909.69852	229.36	13.41
2458909.70018	292.78	11.64
2458909.70184	299.48	12.12
2458909.70349	342.46	9.54

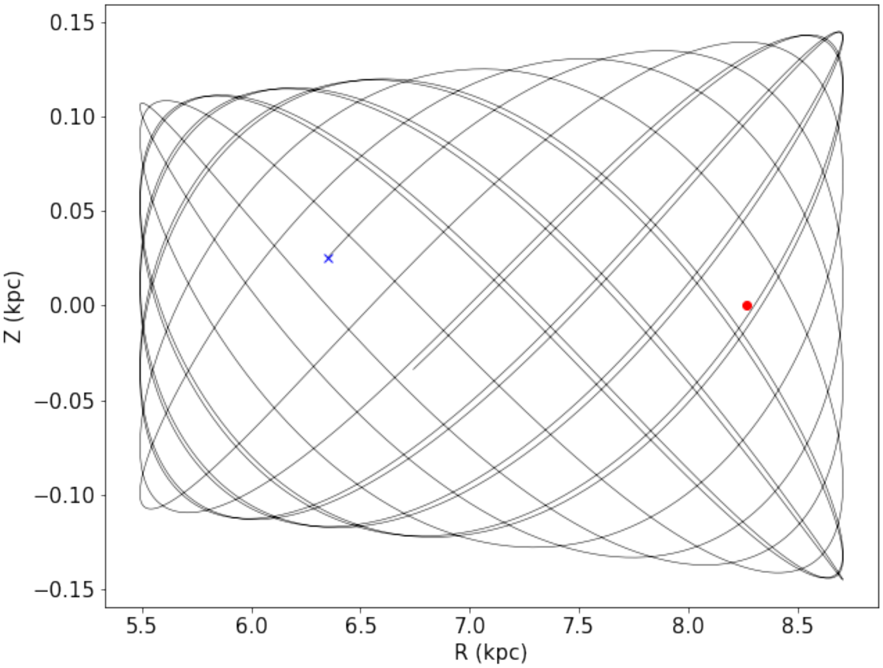

Figure 9. Galactocentric orbit for HD 265435. For illustrative purposes, we used a lookback time of 1 Gyr. We show the height above the disk (Z) as a function of Galactocentric distance $R = \sqrt{X^2 + Y^2}$. The current position of the Sun is indicated with a red dot for reference, and the position of HD 265435 is marked with a blue cross.

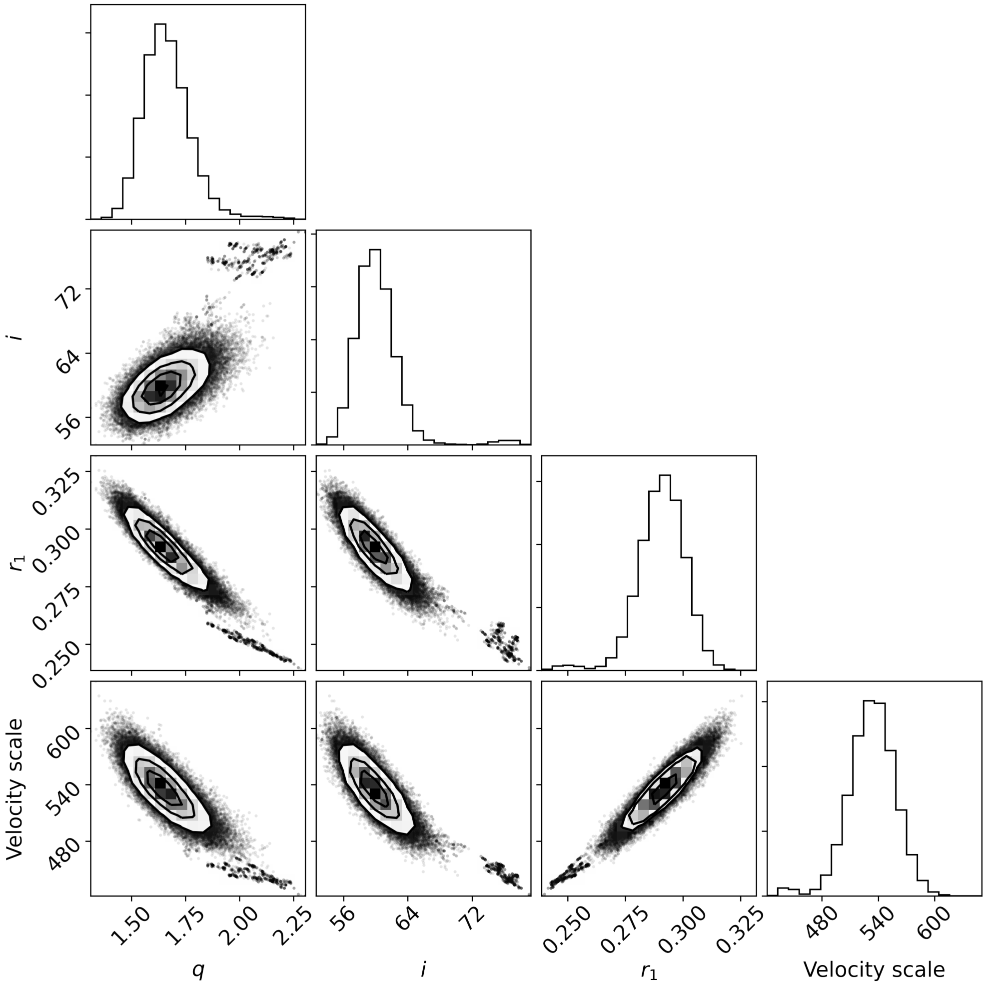

Figure 10. **Corner plot[105] for the MCMC fit of the light curve**.